

Customer	: ESRIN	Document Ref	: SST_CCI-WP100-DMI-201
Contract No	: 4000109848/13/I-NB	Issue Date	: 20 February 2019
WP No	: 100	Issue	: 1

Project : SST CCI Phase-II

Title : Quantification of atmospheric influence on Passive Microwave Observations

Abstract : This document contains the report for WP100 in Phase-II of the SST_cci project.

Author(s) :

Jacob Høyer

Jacob L. Høyer, Tian Tian,
Emy Alerskans and Pia
Nielsen-Englyst, DMI. Leif
Toudal Pedersen, DTU. Sabine
Embacher, Tom Block,
Brockmann Consult GmbH,
Chelle Gentemann, ESR.

Checked by

Chris Merchant

Chris Merchant
Science Leader, UoR
Hugh Kelliher
Project Manager
Space ConneXions Limited

Accepted by :

Craig Donlon
ESA Technical Officer
ESTEC

Distribution : SST_cci team members
ESA (Craig Donlon)

**EUROPEAN SPACE AGENCY
CONTRACT REPORT**

The work described in this report was done under ESA contract.
Responsibility for the contents resides in the author or organisation
that prepared it.

AMENDMENT RECORD

This document shall be amended by releasing a new edition of the document in its entirety. The Amendment Record Sheet below records the history and issue status of this document.

AMENDMENT RECORD SHEET

ISSUE	DATE	REASON FOR CHANGE
0.1	24-10-18	First draft for internal review
1 draft	18-12-18	Final draft for ESA review
1	20-02-19	First Issue

TABLE OF CONTENTS

1. OVERVIEW AND BACKGROUND INFORMATION.....	1
1.1 Introduction.....	1
1.2 Input Data.....	1
1.2.1 CALIPSO Level 2 Cloud Product.....	1
1.2.2 MODIS Level 2 Cloud Product.....	3
1.2.3 In Situ Drifter SST.....	4
1.2.4 Observations from AMSR-E.....	4
1.2.5 OE & RE SST Retrievals using AMSR-E Data.....	4
2. ESA-CCI MULTI-SENSOR MATCHUP DATASET (MMD).....	6
2.1 Derived MMD15 Variables	6
2.2 Data Filtering.....	9
2.1 Data Overview.....	11
3. ATMOSPHERIC INFLUENCE ON THE OE AND RE RETRIEVALS	13
3.1 MODIS Cloud Data.....	13
3.2 CLAY Cloud Features and Cloud Phase	14
3.3 VFM Aerosol.....	20
4. RECOMMENDATIONS FOR SCREENING OF THE RETRIEVAL ALGORITHM	22
4.1 Relation to NWP Parameters	22
4.2 Relation between retrieved OE TCLW and TIWP and $N_{\text{pixel_DCC}}$	23
4.3 Uncertainty on SST Retrievals	24
4.4 Ice Impact on Observations.....	26
5. CONCLUSIONS AND RECOMMENDATIONS.....	28
5.1 General Concepts	28
6. REFERENCES.....	30
7. ACKNOWLEDGEMENT TO CLOUD DATA PROVIDERS.....	32

1. OVERVIEW AND BACKGROUND INFORMATION

1.1 Introduction

Satellite-based Passive Microwave (PMW) observations of sea surface temperature (SST) are particularly valuable in cloudy conditions, where infrared observations are not available. PMW observations from instruments like AMSR-E and AMSR-2 have the ability to perform observations in cloudy conditions, but have limitations when e.g. severe rain is present. The exact influences of rain and other atmospheric conditions on the PMW observations and on the SST retrievals have until now not been quantified. Many microwave-based retrievals not only make use of channels below 10 GHz, which carry most of the information about surface properties, but also of the higher frequencies, i.e. 18 GHz, 23 GHz, 37 GHz and some even 89 GHz. The higher frequencies are more strongly influenced by atmospheric compounds such as water droplets and ice crystals. This study examines the influence on different atmospheric effects, such as cloud cover, ice and water content and aerosols, using observations from the CALIOP, which is an active sensor onboard Cloud–Aerosol Lidar and the Infrared Pathfinder Satellite Observations (CALIPSO) instrument, and the Moderate Resolution Imaging Spectroradiometer (MODIS) that were flying in the same satellite constellation as e.g. the AMSR-E satellite (the A-train). A multisensory matchup approach has been followed, where the PMW observations have been matched with in situ observations, and the CALIOP and MODIS products to facilitate the assessment of the impact of these effects.

Two types of SST retrievals are used to test the atmospheric impact: an optimal estimation retrieval and a regression like retrieval, both retrievals have been developed within the ESA CCI SST project with the aim of generating a pilot Climate Data Record (CDR) of SST from AMSR-E and AMSR-2. The outcome of the study will serve to better characterize the PMW based SST observations in regions with e.g. persistent cloud cover, where these observations are the only source of SST information. The findings thus provide an important contribution to understanding PMW SST observations and towards combining PMW and IR satellite records.

The report is structured such that the input data are described in section 1.2 and the generation of the matchup dataset in Section 1.3. Chapter 2 presents the content of the multi-sensor matchup database (MMD) and the analysis of the atmospheric impact is performed in Chapter 3. Recommendations on how to improve retrieval algorithms are found in Chapter 4. Finally, discussion and conclusions are found in Chapter 5.

1.2 Input Data

Several different observations and auxiliary data are used in this study to investigate the performance and the dependencies of the PMW SST retrievals. The main data types and their characteristics are presented in this section.

1.2.1 CALIPSO Level 2 Cloud Product

CALIOP is an active sensor onboard Cloud–Aerosol Lidar and Infrared Pathfinder Satellite Observations (CALIPSO). It is a near-nadir-viewing, polarization-sensitive, elastic backscatter lidar that uses a laser transmitting at dual wavelengths of 1063 nm and 532 nm. The combination of total backscatter radiation measured at 1063 nm and the degree of linear depolarization at 532 nm are used to discriminate between clouds and aerosols (Liu et al. 2009). The lidar surface footprint is 333 m for both cross track and along track and has a vertical resolution of 30m at altitudes below 8.2km. The data are recorded in nominal increments of 15 consecutive laser pulses, which is nominally equivalent to a distance of 5-km along the laser ground-track. Each CALIOP product file covers a 50-minute time interval for half orbit, and approximately 10,000 files are produced yearly.

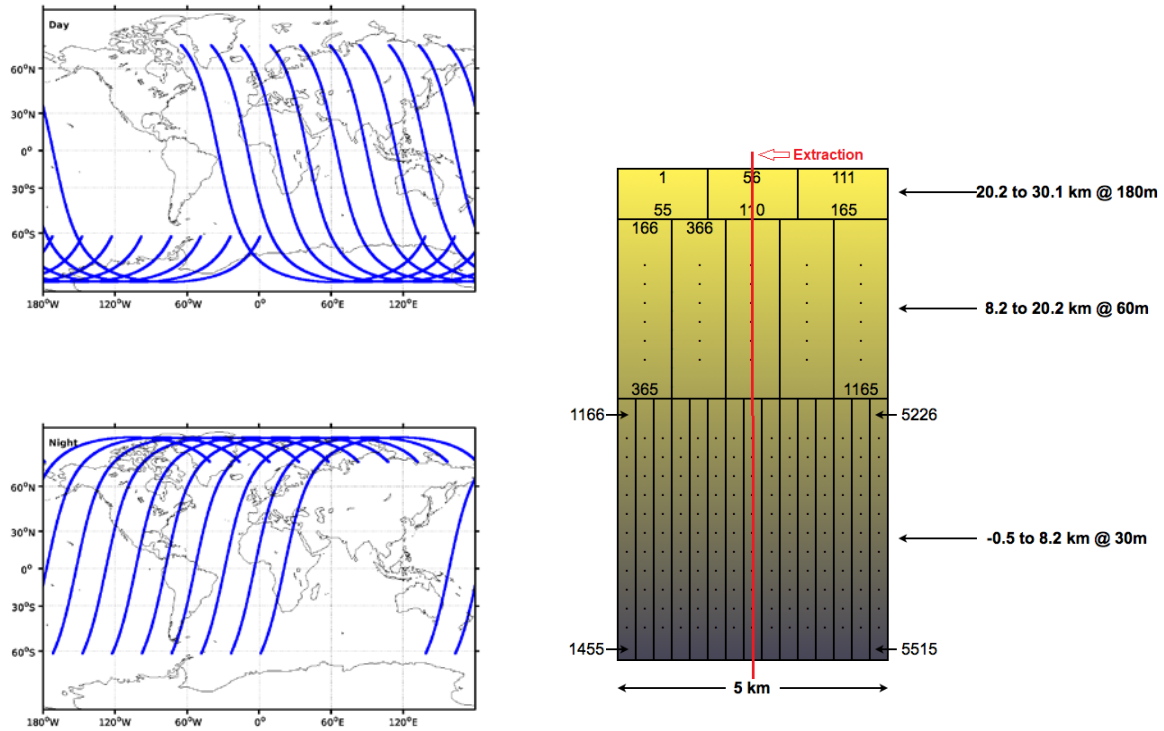


Figure 1-1: Left panels: examples of the first 10 CALIPSO orbital ground tracks on 2018-01-01 in the day and night portions, respectively. Right panel: example of CALIOP-VFM horizontal resolution (along-track) of 5 km and vertical resolution of 30 m, 60m and 180m at altitudes below 8.2 km, 20.2 km and 30.1 km, respectively. The red line shows that the horizontal midpoints from each vertical layer are extracted to represent one pixel.

Table 1-1: The vertical and horizontal resolution of the CALIOP VFM data.

Profile spatial resolution					
Altitude region		Vertical resolution (meters)	Horizontal resolution (meters)	Profiles per 5 km	Samples per profile
Base (km)	Top (km)				
-0.5	8.2	30	333	15	290
8.2	20.2	60	1000	5	200
20.2	30.1	180	1667	3	55
Total					545

The standard version 4.10 Level 2 lidar vertical feature mask (CAL_LID_L2_VFM) product was used and the data product provides feature classification within a vertical profile. As shown in Table 1-1 (also see Figure 1-1), the vertical and horizontal resolution of the profile varies as a function of altitude above mean sea level (Hunt et al., 2009). For each layer detected in the CALIOP backscatter data, a set of feature classification flags are derived to represent (a) feature type (e.g., cloud, aerosol, stratospheric layer); (b) feature subtype; (c) layer ice-water phase (clouds only); and (d) the amount of horizontal averaging required for layer detection. Note that, if the feature type (a) is detected as cloud, the cloud type can be further acquired from feature subtype (b), such as low overcast (transparent), low overcast (opaque), transition stratocumulus, low, broken cumulus, altocumulus (transparent), altostratus (opaque), cirrus (transparent) and deep convective (opaque).

For the cloud layer analysis, the lidar Level 2, 5 km cloud layer product (CAL_LID_L2_05km CLay) version 4.10 was used. The cloud layer products were built around two tightly coupled data types. The first of these is a set of column properties, which describe the temporal and spatial location of the vertical column of atmosphere being sampled. Column properties include satellite position data and viewing geometry, information about the surface type and lighting conditions, and the number of features (e.g., cloud and/or aerosol layers) identified within the column. For each set of column properties, there is an associated set of layer properties. These layer properties specify the spatial and optical characteristics of each feature found (e.g. opacity flag), and include quantities such as layer base and top altitudes, optical depth, layer-integrated ice water path.

While the 5 km layer products are reported on a uniform 5 km grid, the amount of horizontal averaging required to detect a layer may exceed 5 km. For example, detection of subvisible cirrus during daylight operations may require averaging to 20 km or even 80 km horizontally. In these cases, the layer properties of the feature detected are replicated as necessary to span the full extent of the averaging interval required for detection. The maximum number of layers reported per profile in the cloud layer products is 10.

The fundamental data product is the vertical location of cloud and aerosol layer boundaries. All other layer properties, such as integrated ice water path, are computed with reference to these boundaries. Clouds and aerosols are reported separately in the CALIOP layer products. Stratospheric features are recorded in the 5 km aerosol product. In this analysis we did not use the aerosol layer products, only the cloud layer products.

1.2.2 MODIS Level 2 Cloud Product

The Moderate Resolution Imaging Spectroradiometer (MODIS) is an imaging radiometer that measures radiances at 36 wavelengths with centre wavelengths ranging from the visible to thermal infrared (0.413–14.235 μm) and spatial resolution from 250 m to 1 km. One of its advantages is its high spatial resolution that provides larger statistics and a more comprehensive cloud map compared to that of active sensors. The MODIS cloud detection algorithm (Ackerman et al. 1998; Frey et al. 2008) uses a fuzzy-logic scheme to quantify whether a spectral test categorizes a particular field of view (FOV) to be confidently cloudy, probably cloudy, probably clear, or confidently clear. The MODIS cloud product combines infrared and visible techniques to determine both physical and radiative cloud properties. MODIS infrared channel radiances are used to derive cloud top temperature, cloud top height, effective emissivity, cloud phase (ice vs. water, opaque vs. non-opaque), and cloud fraction under both daytime and nighttime conditions. MODIS visible radiances are used to derive cloud optical thickness and effective particle radius and cloud shadow effects. Near infrared solar reflected radiance provides additional information in the retrieval of cloud particle phase (ice vs. water, clouds vs. snow).

In this study, cloud fraction, cloud phase infrared, cloud optical thickness and cloud mask were taken at a spatial resolution of 5 km from the collection 6 MYD06_L2 product, containing data collected from the Aqua platform (http://modis-atmos.gsfc.nasa.gov/MYD06_L2/). The MYD06_L2 consists of parameters at a spatial

resolution of either 1- km or 5-km (at nadir). For 1-km resolution parameters, such as cloud optical thickness, the nearest-neighbour pixel to the 5 km pixel for other parameters was extracted (Baum et al, 2012). Each MYD06_L2 product file covers a five-minute time interval and approximately 288 files are produced daily. Nighttime files are smaller than their daytime counterparts since only cloud top properties are retrieved at night.

Because MODIS is a passive sensor, it has significant limitations in describing cloud vertical structures with its column-integrated cloud properties such as cloud optical depth, particle effective radius, and cloud top effective temperature (Chang and Li, 2005; Davis et al., 2009; Sourdeval et al., 2013).

1.2.3 In Situ Drifter SST

The in situ dataset is composed of measurements from the International Comprehensive Ocean-Atmosphere Dataset (ICOADS) version 2.5.1 (Woodruff et al., 2011), and the Met Office Hadley Centre (MOHC) Ensemble dataset version 4.2.0 (EN4, Good et al., 2013). Measurements from drifting buoys constitute the main source of observations. Drifting buoys measure the temperature, typically hourly, from a sensor at about 20 cm depth in calm waters and the uncertainty from sensor calibration is inferred to about 0.2 °C (O'Carroll et al., 2008). MOHC provides quality control flags and track flags (Atkinson et al., 2014).

1.2.4 Observations from AMSR-E

JAXA's AMSR-E instrument was launched in May 2002 on NASA's Aqua satellite. The AMSR-E instrument is a conical scanning microwave imaging radiometer that measures both vertical and horizontal linear polarizations at 6.9, 10.7, 18.7, 23.8, 36.5, and 89.0 GHz channels using an antenna diameter of 1.6 m. For a detailed description of the AMSR-E instrument, see e.g. Wentz and Meissner, 2000. In this study we use the spatially resampled L2A swath data product AMSR-E V12 (Ashcroft and Wentz, 2013) produced by Remote Sensing Systems (RSS) and distributed by NASA's National Snow and Ice Data Center (NSIDC; https://nsidc.org/data/ae_l2a). The RSS L2A product includes brightness temperatures for all AMSR-E channels re-sampled to the resolution of other channels and the location where the reflection vector intersects the geostationary sphere, used for development of RFI flagging. Sun glint angles are also calculated as a part of the RSS L2A AMSR-E V12 files. For this analysis, we use the re-sampling to 6.9 GHz resolution for the 5 lowest frequencies. This implies that all observations have a resolution footprint of 75 x 43 km, but come in the data set with a spatial grid resolution of 10 km.

1.2.5 OE & RE SST Retrievals using AMSR-E Data

The retrieval of SST is achieved using two different algorithms. The first algorithm uses the Optimal Estimation (OE) technique to retrieve subskin SST from AMSR-E observations (Nielsen-Englyst et al., 2017). The OE method retrieves the minimum posterior error variance estimate of the ocean and atmosphere (the state vector) by inverting a forward model based on a slightly updated version of the physical surface emissivity and a radiative transfer model described in Wentz et al. 2000. The OE algorithm only uses the 10 lowest AMSR-E channels; 6.9, 10.7, 18.7, 23.6, and 36.5 GHz (horizontal and vertical polarization). The forward model predicts the top-of-atmosphere microwave brightness temperatures that should be measured by the individual channels given knowledge of the relevant geophysical parameters of the ocean and atmosphere. Four geophysical parameters are considered to be the leading terms controlling the observed microwave brightness temperatures and these are referred to as the state vector: wind speed (WS), integrated columnar atmospheric water vapour content (TCWV), total cloud liquid water (TCLW) and sea surface temperature (SST). In OE, a priori information about the expected mean and covariance of the geophysical parameters can be used to put restrictions on the variances of the retrieved geophysical parameters. In this case, the prior information is NWP fields. OE can be considered to be an adjustment of the a priori state vector based on

the difference between simulated and observed brightness temperatures. The method takes appropriate account of errors by combining the a priori state vector and the information content in the observed brightness temperatures. Nielsen-Englyst et al., 2018 found that the performance of the SST retrievals is closely related to OE's ability to reproduce the observed brightness temperatures. This information was used to estimate the uncertainty of the individual SST retrievals based on a scaled root mean square difference of the observed minus simulated brightness temperatures ($RMSE_{TB}$), using a scaling factor of 0.55.

The second algorithm used to retrieve SST is a two-step multiple linear regression (RE) model with localized algorithms (Alerskans et al., 2018). In the first step of the regression retrieval algorithm, an initial SST is obtained through the use of localized latitude and satellite orbit algorithms. The data is divided into latitude and orbit bins, defined for latitudes in the interval -90 to 90° , with a bin size of 2° , and for descending (0) or ascending (1) satellite orbit. Hence, the first step consists of 182 localized latitude and orbit retrieval algorithms, each using a different set of regression coefficients. The initial estimate of SST is then used in the second step of the regression retrieval algorithm, where a final SST is obtained through the use of localized SST and wind speed algorithms. For this step, the data is divided into SST and wind speed bins, defined for SSTs in the interval -2 to 34°C , with a bin size of 2°C , and for wind speeds in the interval 0 to 20 ms^{-1} , with a bin size of 2 ms^{-1} . The second step therefore consists of 209 localized SST and wind speed algorithms. The same SST algorithm formulation is used for both steps and it uses 12 AMSR-E brightness temperature channels; 6.9, 10.7, 18.7, 23.6, 36.5 and 89.0 GHz (dual polarization), incidence angle, wind speed and the relative angle between satellite azimuth angle and wind direction to retrieve SST. A corresponding SST uncertainty is estimated for each retrieval. Within the ESA CCI SST project, the total uncertainty can be divided into three components; a random uncorrelated component, a local systematic component and a global systematic component. Both the local systematic uncertainty and the random uncertainty are estimated using a regression model, which uses retrieved SST, wind speed, solar zenith angle and latitude to retrieve the two SST uncertainty components. In this case, the global systematic effects are deemed to be less than 0.1°C and can be neglected.

2. ESA-CCI MULTI-SENSOR MATCHUP DATASET (MMD)

The concept of MMD has been used within the ESA CCI SST project as datasets used for SST algorithm development and validation (Block et al., 2018; Nielsen-Englyst et al., 2018). The satellite versus in situ matches are constrained by a maximally allowed geodesic distance and a maximal time difference. The same approach was applied to generate the MMD15 which is used in this study here. The MMD15 contains the in situ observations from drifting buoys matched with the orbital Level 2 observations from AMSR-E (primary) and the CALIOP and MODIS as the secondary datasets (Block, 2018).

The Multi-sensor Matchup System software reads in all the in situ observations and finds the corresponding matching satellite observations throughout the full dataset. Matches between the in situ measurement and the primary sensor were only included within a maximal geodesic distance of 20 km and a time difference of maximally 4 h. Furthermore, a maximal distance of 3.54 km (i.e. $\sqrt{2}$ times 2.5 km, half pixel-width) and a time window of 270 minutes were defined to constrain the matches between the primary and secondary sensors. The spatial distance ensures that the in situ measurement is located within the satellite footprints (see Table 1-2). The temporal distance balances the need for accurate collocated data with the need for a sufficient number of useable matches.

The collocated AMSR-E data include a 21 by 21 pixel window with the matchup location in the centre as well as all variables of the corresponding in situ measurement. The ERA-Interim NWP data, with a spatial resolution of about 80 km, were referenced to each AMSR-E pixel and each in situ measurement and spatially interpolated to the data raster. This ancillary information includes a subset of the available ERA-Interim variables, covering a time range of -60 h to +36 h around the matchup time. Processing of the matchup dataset has been performed on the Climate and Environmental Monitoring from Space Facility (CEMS) computing facility at the Centre for Environmental Data Analysis (CEDA). The pixel windows of data extraction for the cloud data are given in Table 2-1. Both MODIS and CALIOP data are at the same resolution of 5 km along the laser ground-track and a size of 21 pixels are equivalent to a distance of approx. 1 degree.

Table 2-1: Pixel window size of data extraction. x is cross-track and y is along-track.

	AMSR-E	MODIS	VFM	CLAY
Extraction window (x by y)	21 by 21	21 by 21	1 by 21	1 by 21

Two different databases were designed; one with MODIS cloud data included in the matchup and one without MODIS cloud data included. In the case where MODIS data were included, the MMD consists of data from in situ drifters, AMSR-E, MODIS and CALIOP VFM and CLAY from 2008 and 2009. We will refer to this MMD as the CALIOP-MODIS matchup. In the other case, the MMD does not include MODIS cloud data and covers a 5-year period from 2007-2011. We will refer to this MMD as the CALIOP matchup.

2.1 Derived MMD15 Variables

The footprint size of the AMSR-E 6.9 GHz resolution is 75 x 43 km whereas the footprint size of both the MODIS product and the CALIOP Lidar (i.e. CALIOP) products are 5 x 5 km and 5 km, respectively. The difference in footprint sizes needs to be taken into account when performing the analysis of the effect of clouds and aerosols on the PMW retrievals. Therefore, averages and standard deviations are calculated for a selected number of variables for a pixel extract of 15 x 9 pixels (75 x 45 km) for MODIS MYD06 variables and 15 pixels (75 km) for CALIOP variables. In addition, the number of pixels in the pixel extract

with a value in the valid range for the variable in question is calculated. The derived MMD15 variables are listed in Table 2-2.

When calculating the horizontal averages (μ) and standard deviations (σ), two different methods are used depending on the variable. In the first approach, averages and standard deviations are calculated over the whole pixel extract, whereas in the second approach, averages and standard deviations are calculated over the number of pixels in the pixel extract with a value in the valid range for the variable in question. As an example of a pixel-extract average, consider the MYD06 variable Cloud Fraction. The average is calculated by:

$$\mu_{EXT} = \frac{sum_H(\text{Cloud Fraction})}{N_{Extract}}$$

where sum_H represents the horizontal sum across the pixel extract and $N_{Extract} = 135$ and denotes the total number of pixels in the pixel extract. As an example of a pixel average, consider the CLAY variable Layer Top Altitude, from which the derived MMD15 variable Cloud Top Height (CTH) is calculated (see Table 1-3). The CTH average is calculated by:

$$\mu_{PIX} = \frac{sum_H(\text{Cloud Top Height})}{N_{Pixel}}$$

where sum_H represents the horizontal sum across the pixel extract and N_{Pixel} denotes the number of pixels in the pixel extract with a valid cloud top height value.

Table 2-2: Key MMD15 derived variables together with the already-existing MMD variables from which they were calculated and which specific flags/conditions were used to calculate them. The number of pixels for the CALIOP variables is defined per pixel, meaning that even if e.g. one pixel contains two clouds in two different layers the count would still be one for that pixel.

MMD variable	Derived MMD variables	Comment	Flagging
MYD06 Cloud Fraction	<ul style="list-style-type: none"> μ_{EXT} σ_{EXT} N_{Pixel} 	Fill value = 0	None
MYD06 Cloud Optical Thickness	<ul style="list-style-type: none"> μ_{EXT} σ_{EXT} N_{Pixel} 	Fill value = 0	<ul style="list-style-type: none"> MYD06 Cloud Optical Thickness ≤ 100; and MYD06 Cloud Optical Thickness Uncertainty ≤ 200
MYD06 Cloud Phase Infrared	No. of pixels with clear sky	Range: [0-135]	<ul style="list-style-type: none"> MYD06 Cloud Phase Infrared = 0
MYD06 Cloud Phase Infrared	No. of pixels with water clouds	Range: [0-135]	<ul style="list-style-type: none"> MYD06 Cloud Phase Infrared = 1
MYD06 Cloud Phase Infrared	No. of pixels with ice clouds	Range: [0-135]	<ul style="list-style-type: none"> MYD06 Cloud Phase Infrared = 2 (ice) or = 3 (mixed ice)

MMD variable	Derived MMD variables	Comment	Flagging
CALIOP VFM Center Feature Classification Flags (CFCF) Type	No. of pixels with aerosols	Range: [0-15] One count per pixel	<ul style="list-style-type: none"> CALIOP VFM CFCF Type = 3 (aerosol)
CALIOP CLAY Feature Classification Flags (FCF) Type	No. of pixels with clear sky	Range: [0-15] One count per pixel	<ul style="list-style-type: none"> $\max_V(\text{CALIOP CLAY FCF Type } 1 \text{ (clear sky conditions)})$
CALIOP CLAY Feature Classification Flags (FCF) Type	No. of pixels with clouds	Range: [0-15] One count per pixel	<ul style="list-style-type: none"> CALIOP CLAY FCF Type = 2 (cloud)
CALIOP CLAY Feature Classification Flags (FCF) Subtype	No. of pixels with deep convective clouds	Range: [0-15] One count per pixel	<ul style="list-style-type: none"> CALIOP CLAY FCF Subtype = 7 (deep convection)
CALIOP CLAY Feature Classification Flags (FCF) Type	No. of pixels with ice clouds	Range: [0-15] One count per pixel	<ul style="list-style-type: none"> CALIOP CLAY FCF Type = 2 (cloud); and CALIOP CLAY FCF Ice Water Phase = 1 (ice) or = 3 (mixed ice)
CALIOP CLAY Feature Classification Flags (FCF) Type	No. of pixels with opaque clouds	Range: [0-15] One count per pixel	<ul style="list-style-type: none"> CALIOP CLAY FCF Type = 2 (cloud); and CALIOP CLAY Opacity Flag = 1
CALIOP CLAY Feature Classification Flags (FCF) Type	No. of pixels with transparent clouds	Range: [0-15] One count per pixel	<ul style="list-style-type: none"> $N_{clouds} - N_{opaque\ clouds}$
CALIOP CLAY Ice Water Path (IWP)	Total ice water content (TIWP) <ul style="list-style-type: none"> μ_{EXT} σ_{EXT} N_{pixel} 	$TIWP = \sum_V(IWP)$ Fill value = 0 Range N_{pixel} : [0-15]	<ul style="list-style-type: none"> CALIOP CLAY IWP ≥ 0, CALIOP CLAY IWP Uncertainty ≤ 99.9, CALIOP CLAY FCF Type = 2 (cloud); and CALIOP CLAY FCF Ice Water Phase = 1 (ice) or = 3 (mixed ice)
CALIOP CLAY Ice Water Path (IWP)	TIWP without deep convection <ul style="list-style-type: none"> μ_{EXT} σ_{EXT} N_{pixel} 	$TIWP = \sum_V(IWP)$ Fill value = 0 Range N_{pixel} : [0-15]	Same flags as for TIWP <ul style="list-style-type: none"> CALIOP CLAY FCF Subtype $\neq 7$ (deep convection)
CALIOP CLAY Layer Top Altitude (LTA)	Cloud Top Height (CTH) <ul style="list-style-type: none"> μ_{PIX} σ_{PIX} N_{pixel} 	$CTH = \max_V(LTA)$ Range N_{pixel} : [0-15]	<ul style="list-style-type: none"> CALIOP CLAY LTA > 0; and CALIOP CLAY FCF Type = 2 (cloud)

MMD variable	Derived MMD variables	Comment	Flagging
CALIOP CLAY Layer Top Altitude (LTA)	CTH Opaque <ul style="list-style-type: none"> • μ_{PIX} • σ_{PIX} • N_{pixel} [0-15] 	CTH Opaque = $\max_V(LTA_{opaque})$ Range N_{pixel} : [0-15]	Same flags as for CTH and <ul style="list-style-type: none"> • CALIOP CLAY Opacity Flag = 1
CALIOP CLAY Layer Top Altitude (LTA)	CTH Opaque without deep convection <ul style="list-style-type: none"> • μ_{PIX} • σ_{PIX} • N_{pixel} 	CTH Opaque no Deep Convection = $\max_V(LTA_{op, no DC})$	Same flags as for CTH Opaque and <ul style="list-style-type: none"> • CALIOP CLAY FCF Subtype $\neq 7$ (deep convection)

2.2 Data Filtering

The quality of satellite observations, in situ measurements and auxiliary information is very important for the accuracy and performance of the retrieval algorithm. If erroneous data are included, it will lead to an erroneous SST retrieval. Hence, the data need to be quality-controlled and filtered for various surface and atmospheric effects.

Data were flagged as erroneous if the AMSR-E pixel or scan quality were set to fail or if the brightness temperature fell outside the normal range (0-320 K). In addition, data were flagged if the in situ data seemed to be erroneous and had not passed the quality control. Data were also flagged if the in situ or NWP SST was less than $-2\text{ }^{\circ}\text{C}$ or greater than $34\text{ }^{\circ}\text{C}$ or if NWP wind speed was greater than 20 m s^{-1} . Together, these quality controls represent a gross error check. In addition to the gross error check, flagging were performed to account for various surface and atmospheric effects that could compromise the SST retrieval. Data were flagged for land contamination based on the AMSR-E land/ocean flag and for sea ice contamination based on the NWP sea ice fraction. Furthermore, data were flagged for sun glitter contamination if the sun glint angle was less than 25° . Data were flagged for RFI contamination using Table 1-2 by Gentemann and Hilburn (2015) together with observation location and geostationary reflection longitude and latitude. As a last quality control for the in situ data, a $3\text{-}\sigma$ filter was used on the NWP and in situ SST difference to remove erroneous in situ observations.

Flagging was also performed for the PMW SST retrievals. If the retrieved SST were outside the accepted range (-2 to $34\text{ }^{\circ}\text{C}$), the data were flagged as erroneous. For the OE retrievals, an additional filter was added on the RMSE for the observed minus simulated brightness temperatures, $RMSE_{TB}$, which is an indicator of how well the OE algorithm is able to reproduce the observed brightness temperatures. Nielsen-Englyst et al. 2018 found that the performance of the SST retrieval is closely related to the $RMSE_{TB}$ value. Here, data were flagged as erroneous if $RMSE_{TB} > 5$, which is larger than in Nielsen-Englyst et al., to allow for atmospheric effects to be included in the matchup dataset. Finally, the number of matchups per degree of latitude was restricted to 100 and 500 matchups for the CALIOP-MODIS and CALIOP datasets, respectively, to ensure that the analysis results are based upon a latitudinal representative dataset.

Table 2-3: Number of matchups and percentage of matchups removed by each data filtering step for the OE analysis. ¹The percentage of gross error checked matchups removed by applying each filter individually. ²The percentage of matchups removed by applying the filter is calculated from the number of matchups that passed the “All above checks” option. ³The percentage of matchups removed by the filter is from the number of matchups that passed the “All checks” filtering.

Flagging	CALIOP-MODIS		CALIOP	
	N	% removed	N	% removed
<i>None (all matchups)</i>	58,326		52,720	
<i>Gross error check</i>	51,066	12.4	48,948	7.2
<i>Land mask¹</i>	38,781	24.1	41,129	16.0
<i>Sea ice mask¹</i>	32,681	36.0	39,697	18.9
<i>Sun glitter¹</i>	51,066	0.0	48,942	0.012
<i>RFI¹</i>	50,139	1.8	46,873	4.2
All above checks	28,606	51.0	35,144	33.3
<i>3σ filter on NWP minus in situ SST difference²</i>	28,310	1.0	34,586	1.6
<i>RMSE_{TB}²</i>	28,300	0.02	34,536	0.1
All checks	28,300	51.5	34,536	34.5
<i>Even out data by latitude³</i>	8,629	69.5	29,154	15.6
Total	8,629	85.2	29,154	44.7

2.1 Data Overview

The number of matchups after each step in the data filtering procedure and the percentage of matchups the filter removes is shown in Table 2-3. The final number of matchups used for the analysis with the CALIOP dataset is 29,154 for the OE algorithm and 29,201 for the RE algorithm whereas for the analysis with the CALIOP-MODIS dataset it is 8,629 for both the OE and RE algorithms (Table 2-3). Figure 2-1 shows the geographical and latitudinal distribution of filtered matchups for the two datasets used for the OE analysis. The distributions of matchups, used for the RE analysis, are not shown because they are similar to the distributions for the OE analysis. The distribution of matchups by year for the CALIOP and CALIOP-MODIS datasets is shown in Figure 2.2. In the CALIOP-MODIS dataset, year 2009 consists of approximately 1,000 more matchups than year 2008 and in the CALIOP dataset, year 2010 consists of roughly 8,350 matchups whereas the other years consist of approximately 5,000-6,000 matchups each.

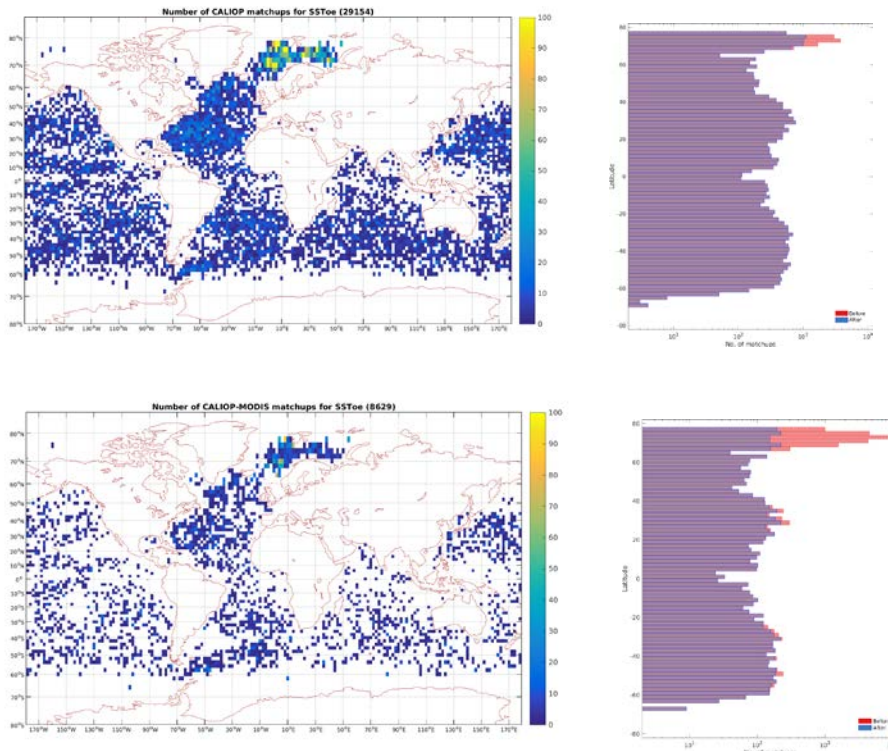


Figure 2-1: Geographical distribution of the number of satellite vs in situ matchups gridded in 2x2 deg (left panels) and the latitudinal distribution (right panels) before and after the matchups have been evened out by latitude for the OE algorithm analysis (red in left panel indicate the removed data): the CALIOP matchups (top) and CALIOP-MODIS matchups (bottom).

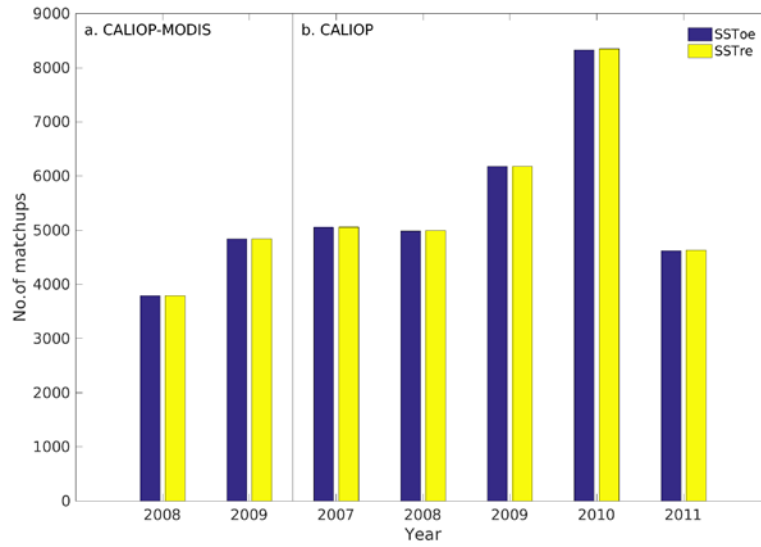


Figure 2-2: Distribution of satellite vs. in situ matchups by year: a. the CALIOP-MODIS matchup dataset (2008-2009) and b. the CALIOP matchup dataset (2007-2011).

3. ATMOSPHERIC INFLUENCE ON THE OE AND RE RETRIEVALS

The performance of the OE and RE retrieved SSTs compared to in situ SSTs is shown in Table 3-1 for the two datasets. In general, the retrieved SSTs are slightly colder than the in situ SSTs with standard deviations ranging from 0.56 to 0.66 °C (highest for the RE algorithm).

The impact of the different atmospheric parameters on the PMW SST retrievals is investigated in this section through the assessment of the SST retrieval performance as a function of each of the parameters. The atmospheric variables shown in this section are:

- Cloud fraction (from MODIS)
- Total ice water content (TIWP)
- Opaque cloud top height (OCTH)
- Number of pixels with deep convection ($N_{\text{pixel_DCC}}$)
- Number of pixels with aerosols ($N_{\text{pixel_AERO}}$)

Note that the performance of the SST retrievals was examined for all variables listed in Table 3. We have chosen to show here only the results where we see some effects on the SST retrievals or if it is a widely used auxiliary data set, such as for the MODIS cloud cover data set.

3.1 MODIS Cloud Data

For the CALIOP-MODIS dataset, we focused on the relationship between the retrieved minus in situ SST differences and the MODIS cloud variables, such as cloud fraction, cloud optical thickness and the number of pixels, in the pixel extract containing water clouds or ice clouds. Generally, the impact is small and the SST performance does not vary much with the value of the cloud variables. As an example, Figure 3-1 shows the retrieved SST minus in situ SST as a function of MODIS cloud fraction. Only a relatively small effect (0.02K for OE and 0.11K for regression) on the average SST performance is found during overcast conditions, i.e. cloud fraction = 0 versus cloud fraction = 1. These differences between cloudy and cloud-free performance are not significant to the 95 % confidence interval for the OE and the regression retrievals due to the small sample size for cloud free conditions and we can therefore not determine any significant impact of the cloud cover (seen from MODIS) on the PMW SST performance.

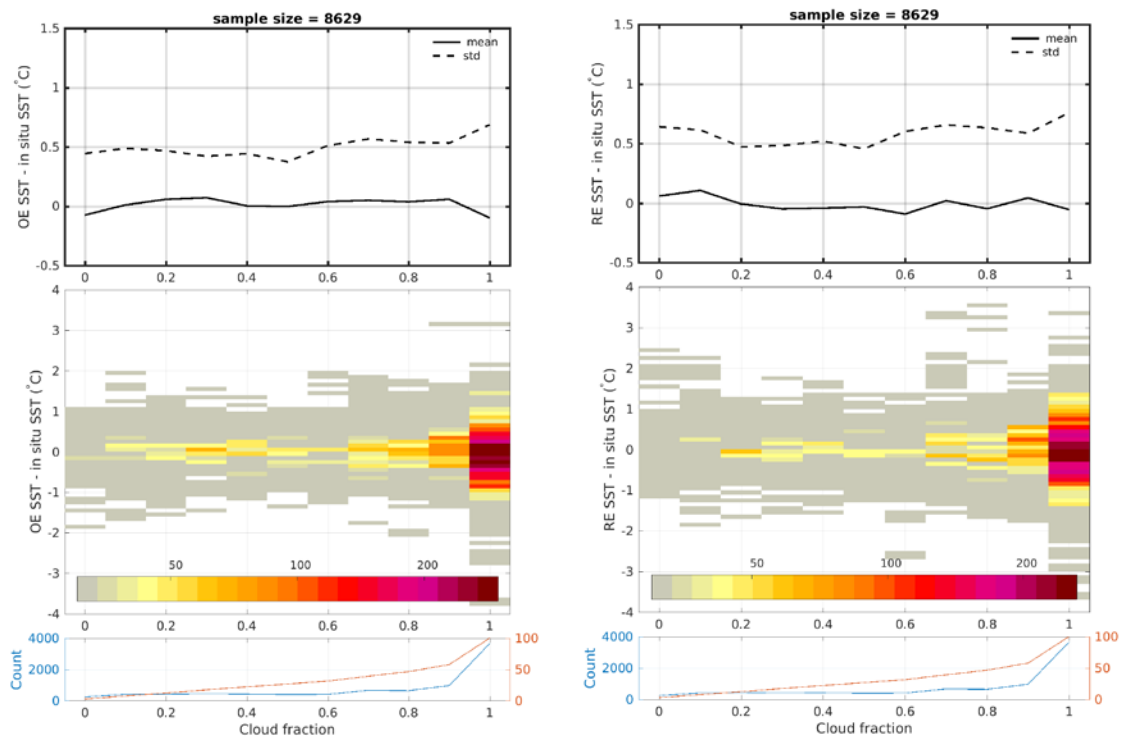


Figure 3-1: Retrieved SST minus in situ SST as a function of MODIS cloud fraction from 2008-2009: OE SST (left) and RE SST (right). Top panels: solid and dashed lines are mean and standard deviation of retrieved SST versus in situ, respectively. Middle panels: number of matchups in each bin. Bottom panels: the total number of matchups (blue) and the cumulative percentage of matchups (red) for each cloud fraction bin. A minimum of 30 matchups in each bin is applied for statistics calculation in the top figures.

3.2 CLAY Cloud Features and Cloud Phase

From the 5-year CALIOP matchup dataset, we extracted subsets of various cloud types and defined several new variables to quantify the cloud features in order to investigate cloud effects on the retrieved minus in situ SST difference (Table 2-2). Total ice water content (TIWP) and opaque cloud top height (OCTH) were identified as the two key variables. In order to assess their influence on the SST retrievals, we extracted two subsets from the CALIOP matchups where we only included matchups with TIWP above 0 g m^{-2} and OCTH above 0 km, respectively. In other words, we only considered the matchups detected as either ice or mixed ice cloud for the analysis of the influence of TIWP on the retrieved SST performance. Therefore the subset used to assess the impact of ice and mixed ice clouds consists of 51% of the total matchups for both the RE and OE analysis. For the analysis using OCTH, we only considered the matchups detected as opaque clouds and hence 66% of the total matchups were extracted for the analysis (Table 3-1).

Table 3-1: Comparison of retrieved SSTs against in situ SSTs for various subsets from the CALIOP matchups, using the filters derived from the CLAY and VFM cloud variables (Table 3). The numbers in the first two rows are used as references for the subset assessments and are calculated from all CALIOP-MODIS and CALIOP matchups, respectively. $N_{\text{pixel_DCC}}$ denotes the number of pixels detected as deep convective clouds within one matchup; note that the subset includes all $N_{\text{pixel_DCC}}$ below the threshold, so that the number of the matchups increases with increasing threshold for $N_{\text{pixel_DCC}}$. $N_{\text{pixel_AERO}}$ denotes the number of pixels classified as aerosol within one matchup.

Subset	Mean/K OE- Drifter	Std/K OE- Drifter	Mean/K RE-Drifter	Std/K RE-Drifter	N_match (OE/RE)	
CALIOP-MODIS	-0.022	0.588	-0.025	0.661	8,629/8,629	100%
CALIOP	-0.022	0.559	-0.012	0.640	29,154/29,201	100%
TIWP>0	-0.069	0.621	-0.018	0.687	14,788/14,822	51%
OCTH>0	-0.042	0.609	-0.017	0.687	19,297/19,337	66%
$N_{\text{pixel_DCC}}=0$	0.004	0.496	-0.001	0.583	23,994/24,005	82%
$N_{\text{pixel_DCC}}<4$	0.002	0.503	0.000	0.584	25,416/25,427	87%
$N_{\text{pixel_DCC}}<8$	0.001	0.511	-0.002	0.591	26,492/26,503	91%
$N_{\text{pixel_DCC}}<12$	-0.002	0.517	-0.002	0.600	27,453/27,465	94%
$N_{\text{pixel_AERO}}=0$	-0.135	0.680	-0.054	0.774	6,118/6,148	21%
$N_{\text{pixel_AERO}}=15$	0.012	0.441	-0.017	0.520	7,784/7,790	27%

Figure 3-2 shows the dependence of the SST performance on the vertically integrated TIWP. The retrieved SSTs get increasing colder than in situ SST for higher TIWP values using both the OE and RE algorithms. Similar, the standard deviations increase for with increasing TIWP. The cumulative percentage of matchups with TIWP below 100 g m^{-2} is approximately 90%. The mean and standard deviation of the SST difference within the subsets are -0.069 and 0.621 °C for the OE algorithm and -0.018 and 0.687 °C for the RE algorithm (Table 5).

Figure 3-3 shows that the SST retrieval quality also depends on the OCTH, in particular for opaque cloud top altitudes higher than 6 km. The cumulative percentage of matchups with an OCTH lower than 6 km is approximately 80%. Comparing the mean and standard deviation of the retrieved SST versus in situ SST within the two subsets (see Table 3-1), it can be seen that the OE SST is more sensitive to TIWP than OCTH, whereas the RE SST does not differ between the two subsets. We have also investigated the dependence of the SST difference on the CLAY cloud top height (CTH) but found no relationship between the SST difference and CTH for neither of the two algorithms (not shown).

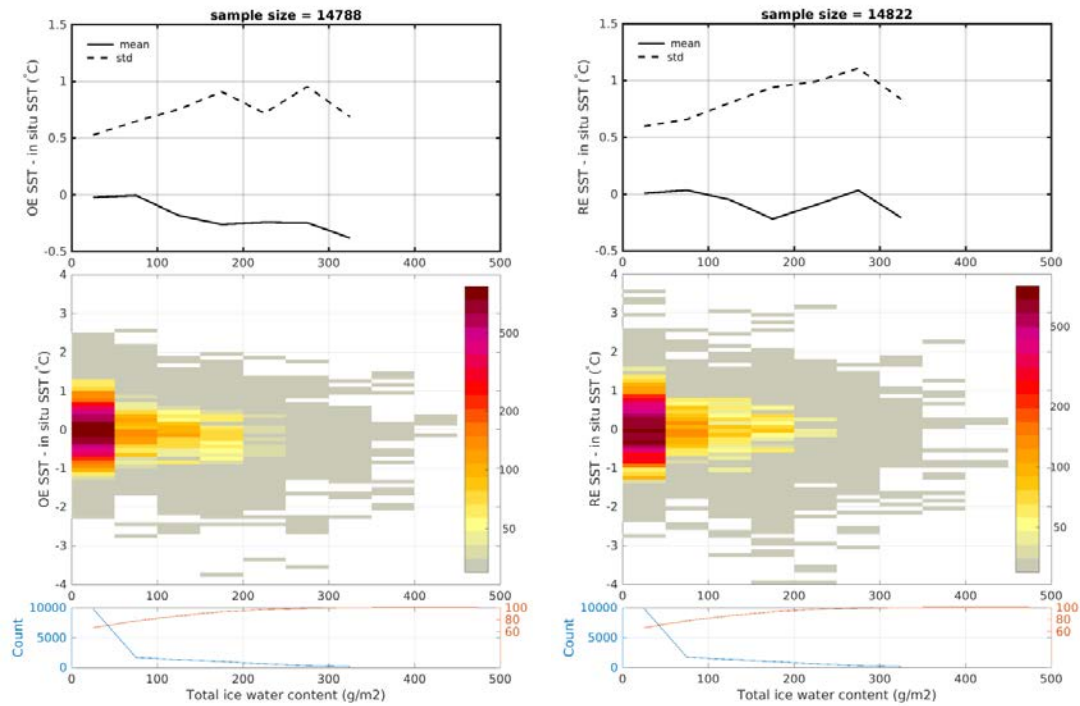


Figure 3-2: Retrieved SST minus in situ SST as a function of TIWP (g m^{-2}) from 2007-2011: OE SST (left) and RE SST (right). Top panels: solid and dashed lines are mean and standard deviation of retrieved SST versus in situ, respectively. Middle panels: number of matchups in each bin. Bottom panels: the total number of matchups (blue) and the cumulative percentage of matchups (red) in each TIWP bin (for 50 g m^{-2}). A minimum of 30 matchups in each bin is applied for statistics calculation in the top figures. Note that this is a subset of the CALIOP matchups, which only includes the matchups detected as either ice or mixed ice cloud with $\text{TIWP} > 0 \text{ g m}^{-2}$. A relation between TIWP and cloud liquid water from NWP are shown in Figure 4.1.

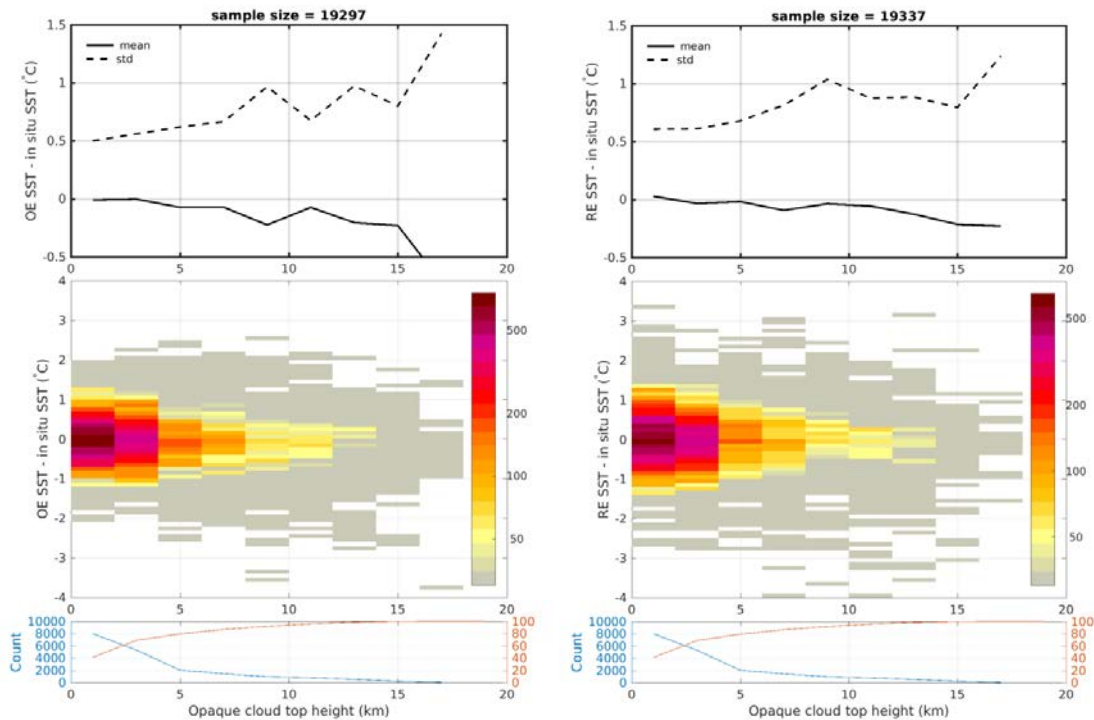


Figure 3-3: Retrieved SST minus in situ SST as a function of OCTH (km) from 2007-2011: OE SST (left) and RE SST (right). Top panels: solid and dashed lines are mean and standard deviation of retrieved SST versus in situ, respectively. Middle panels: number of matchups in each bin. Bottom panels: the total number of matchups (blue) and the cumulative percentage of matchups (red) in each OCTH bin (for 2 km). A minimum of 30 matchups in each bin is applied for statistics calculation in the top figures. Note that this is a subset of the CALIOP matchups, which only includes the matchups detected as opaque cloud with CTH>0 km.

To investigate the effect of rain on the SST retrievals, we extracted the number of pixels containing deep convective clouds (DCCs). The subset without DCCs, which consists of 82% of the total matchups ($N_{\text{pixel_DCC}}=0$ in Table 3-1), was found to have the smallest standard deviation of the retrieved minus in situ SST differences for both retrieval algorithms. By including matchups which contain more DCCs, the variance of the SST differences increased slightly from 0.496 ($N_{\text{pixel_DCC}}=0$) to 0.559 °C (all matches) for the OE analysis and from 0.583 ($N_{\text{pixel_DCC}}=0$) to 0.640 °C (all matches) for the RE analysis. Only 18% of the total matchups contain DCCs (i.e. $N_{\text{pixel_DCC}}>0$), which corresponds to 5,160 and 5,196 matchups for the OE and RE analysis, respectively (Figure 3-4). Limited by such small sample sizes, it is not possible to derive a relation between the number of pixels with DCC and the retrieved SST. However, more than 1,000 matchups within these DCC subsets are detected as fully covered by DCC (i.e. $N_{\text{pixel_DCC}}=15$), and they show relatively large uncertainties compared to the case with matchups detected as covered by 25% of DCC or less (i.e. $N_{\text{pixel_DCC}}<4$), as can be seen in Figure 3-4.

To assess if there were any sampling effects, we investigated the geographical and latitudinal distribution of matchups with $N_{\text{pixel_DCC}}>0$ (Figure 3-5 and Figure 3-6). Figure 3-5 shows that $N_{\text{pixel_DCC}}=15$ is the predominant case in all five zonal regions: in the southern hemisphere (30°S to 90°S), the matchups fully covered by DCC ($N_{\text{pixel_DCC}}=15$) constitutes 25-30% of the total local matchups, whereas between 30°N-60°N, over 20% of the total local matchups are fully covered by DCCs. Therefore, we can conclude that the increased

SST versus in situ differences related to matchups containing DCC, as seen in Figure 3-3, is a general feature and that there is no sampling effect in our analysis.

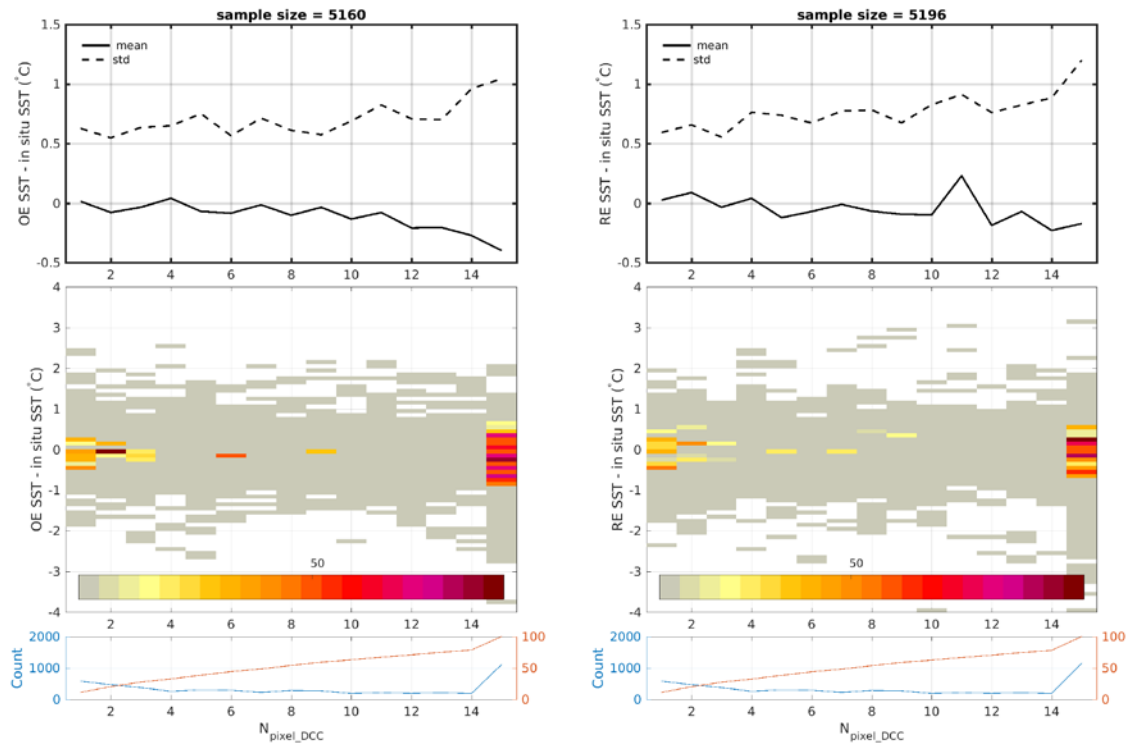


Figure 3-4: Retrieved SST minus in situ SST as a function of number of pixels containing deep convective clouds ($N_{\text{pixel_DCC}}$, ranging from 1 to 15) from 2007-2011: OE SST (left) and RE SST (right). Top panels: solid and dashed lines are mean and standard deviation of retrieved SST versus in situ, respectively. Middle panels: Number of matchups in each bin. Bottom panels: the total number of matchups (blue) and the cumulative percentage of matchups (red) in each bin (for 1 pixel). A minimum of 30 matchups in each bin is applied for statistics calculation in the top figures. Note that 82% of the total matchups are found to have no DCCs (i.e. $N_{\text{pixel_DCC}}=0$) and hence excluded from this figure.

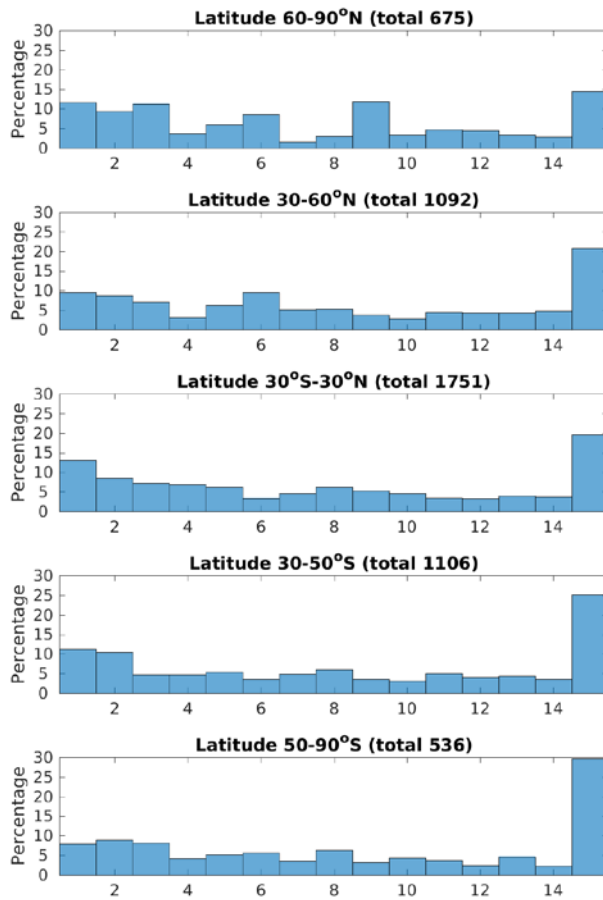


Figure 3-5: Normalised histogram of the number of pixels containing deep convective clouds for OE SST for different latitude bands. The RE SST results were very similar (not shown).

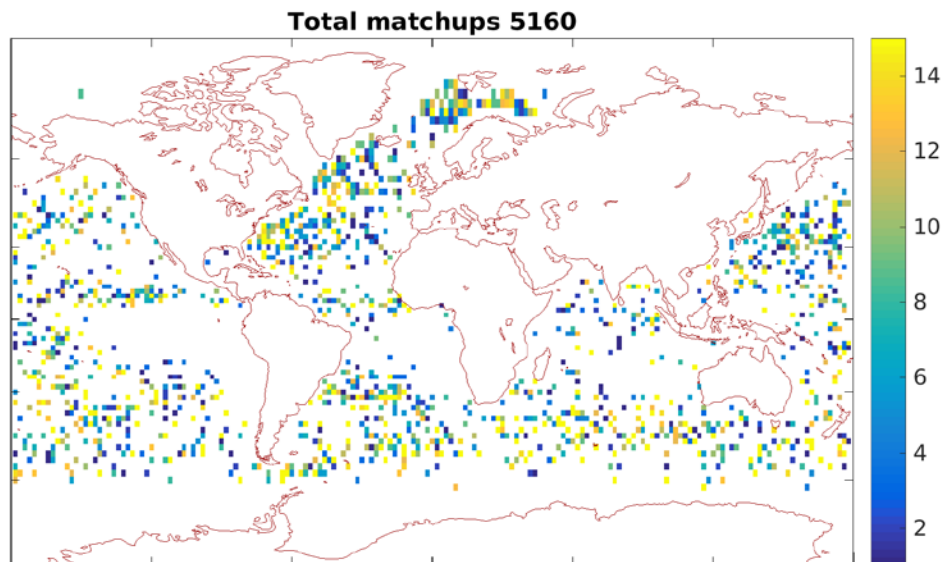


Figure 3-6: Distribution of the number of pixels, ranging from 1 to 15, containing deep convective clouds averaged for 2x2° bins for OE SST. The RE SST results are very similar (not shown).

In order to assess how the SST retrieval quality varies with the occurrence of DCCs, we introduce a filter based on the number of pixels in the pixel extract containing deep convective clouds. Figure 3-7 shows the dependence of the retrieved SST minus in situ SST differences on TIWP and OCTH for five different upper thresholds on the number of DCC within the pixel extract. This way we can choose if we want to use a stricter filter and exclude more matchups or if we want to relax on the strictness of the filter and thus include more matchups so that the number of matchups used in the analysis ranges from a minimum of 9,791 to a maximum of 19,337. Figure 3-7 shows that by gradually removing the effect of DCC, the dependence of the SST difference on TIWP and OCTH gradually decreases. The occurrence of DCC is associated with $TIWP > 200 \text{ g m}^{-2}$ and $OCTH > 6 \text{ km}$.

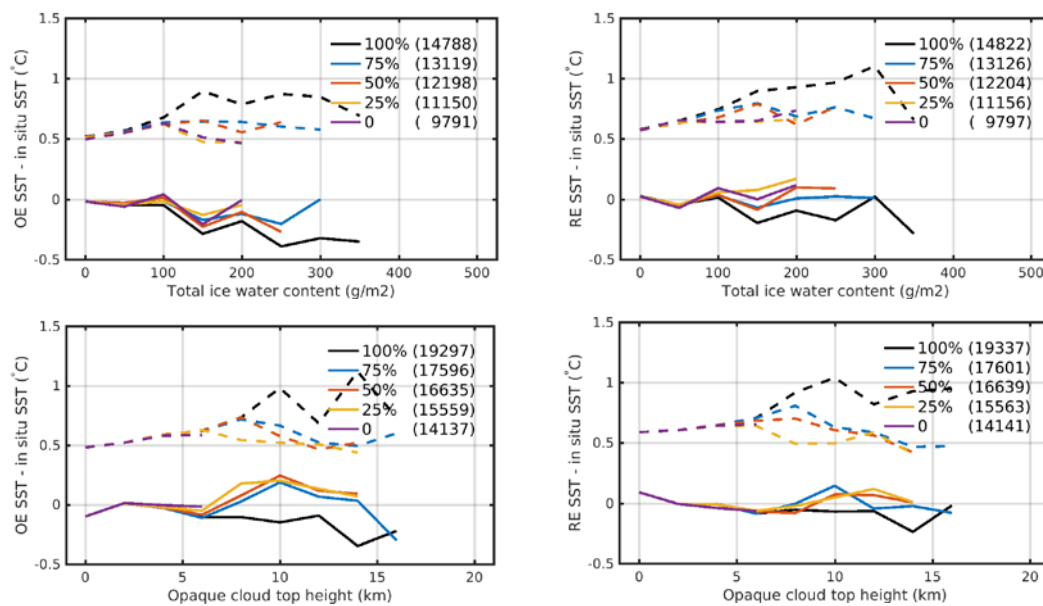


Figure 3-7: Retrieved SST minus in situ SST as a function of TIWP (upper panels) and OCTH (lower panels) for different thresholds of deep convective clouds (DCCs) included and for OE SST (left) and RE SST (right). The five upper thresholds for the maximum number of DCCs in the pixel extract are used: $N_{\text{pixel_DCC}} \leq 0, 3, 7, 11$ and 15 . This is equivalent to 0, 25, 50, 75 and 100% of the pixel extract within a PMW footprint containing deep convective clouds.

3.3 VFM Aerosol

The impact from aerosols on the SST retrievals is shown in Figure 3-8. It is evident that there is no apparent negative influence from aerosols on the quality of the SST retrievals. Conversely, the best performance of both retrievals is actually found for conditions where aerosols are detected in all the CALIOP observations within a PMW satellite footprint, whereas the largest bias and standard deviations are found for aerosol-free pixels. A closer investigation of these results revealed, however, that this dependency is most likely a sampling artefact. Most of the aerosol contaminated matchups are found in warm tropical waters with SSTs above 25°C , whereas the majority of the aerosol-free matchups are located around 70°N where the SSTs are around 5°C . It is well known (and also shown in Nielsen-Englyst et al., 2018) that PMW SST retrievals perform better for warm waters than for cold waters. The aerosol dependency seen in Figure 3-8 is thus not because of aerosols but due to the aerosols being present in regions of warmer water, where the SST retrievals show the best performance. Details are listed in Table 3-1.

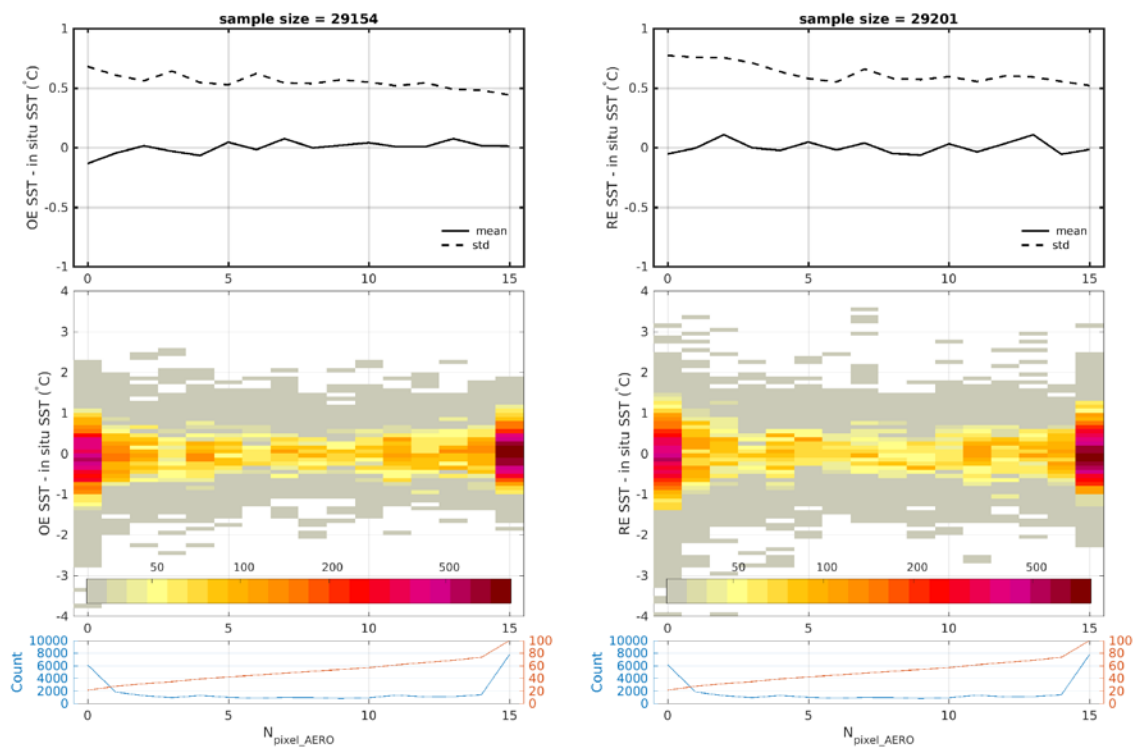


Figure 3-8: Retrieved SST minus in situ SST as a function of number of pixels containing aerosols ($N_{\text{pixel_AERO}}$) from 2007-2011: OE SST (left) and RE SST (right). Top panels: solid and dashed lines are mean and standard deviation of retrieved SST versus in situ, respectively. Middle panels: number of matchups in each bin. Bottom panels: the total number of matchups (blue) and the cumulative percentage of matchups (red) in each bin (for 1 pixel). A minimum of 30 matchups in each bin is applied for statistics calculation in the top figures. Note that the binning of the number of pixels starts from 0, representing aerosol-free matchups, which accounts for 21% of the total matchups.

4. RECOMMENDATIONS FOR SCREENING OF THE RETRIEVAL ALGORITHM

In this section, we aim at identifying the potential of using AMSR-E observations, retrieved variables or NWP fields to identify observations contaminated by atmospheric effects to improve the quality of the SST retrievals. Our analysis in the previous sections showed that whereas the SST retrieval algorithms generally are fairly stable with respect to e.g. cloud cover from MODIS, the analysis against CALIOP observed variables showed that atmospheric effects related to e.g. DCC has a negative impact on the quality of the SST retrievals.

The CALIOP observations are close to nadir observations and it is therefore not feasible to use these observations to perform a quality control of all the AMSR-E retrievals in a swath. In this section we will therefore examine the potential for using auxiliary information to identify and exclude the retrievals where atmospheric effects deteriorate the PMW SST retrievals.

4.1 Relation to NWP Parameters

This section investigates if NWP extracted variables from ERA Interim can be related to the observed atmospheric parameters that influence the PMW SST retrievals. Figure 4-1 shows the relation between the total column cloud ice water (TCIW) and TCLW from NWP and the observed TIWP and $N_{\text{pixel_DCC}}$. It is evident that while there might be a small relation between NWP TCIW and observed TIWP, there is little relation between the NWP TCIW vs. $N_{\text{pixel_DCC}}$ and when NWP TCLW is compared against observed TIWP and $N_{\text{pixel_DCC}}$.

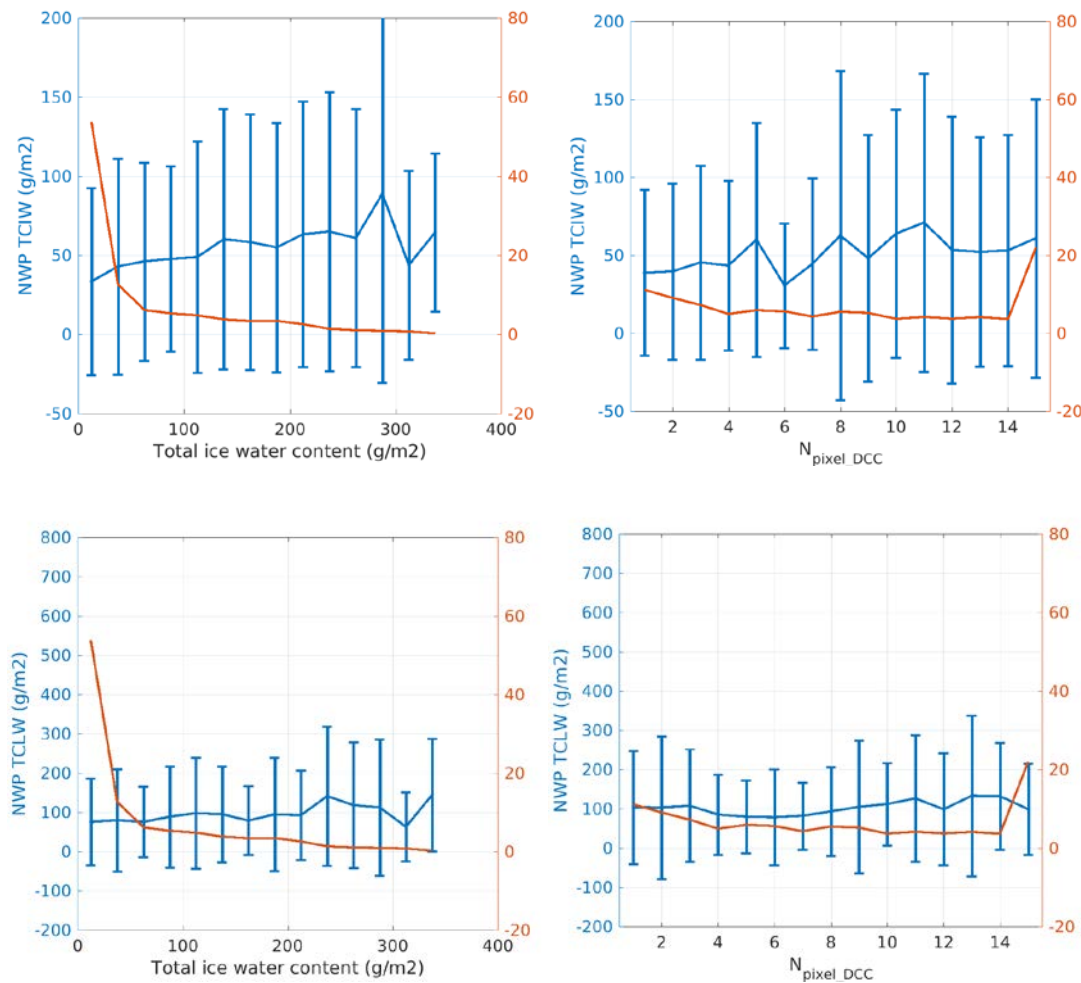


Figure 4-1: NWP Total column cloud ice water (TCIW) (top) and NWP TCLW (bottom) as a function of observed TIWP (left) and number of pixels containing deep convective cloud ($N_{\text{pixel_DCC}}$) (right) from 2007-2011. On the left y-axis: solid lines and error bars represent mean and standard deviation of each bin, respectively. The right y-axis shows normalized percentage of matchups. A minimum of 30 matchups in each bin is applied for statistics calculation.

The results mean that, even though we have demonstrated that high content of TCLW and TCIW influences the quality of the SST retrievals, it is hard to use the NWP for screening the retrievals. This is probably related to the fact that the quality of the NWP TCLW and TCIW variables extracted here is not good enough for this kind of analysis.

4.2 Relation between retrieved OE TCLW and TIWP and $N_{\text{pixel_DCC}}$

TCLW is retrieved simultaneously with the SST in the OE algorithm and can thus potentially be used to identify retrievals affected by severe rain. Here, we examine the relation between the OE retrieved TCLW and the observed TIWP and number of pixels with DCC, $N_{\text{pixel_DCC}}$. The results in Figure 4-2 show a good correlation between the OE TCLW and

TIWP for values less than 150 g m^{-2} . Similarly, there is a relation between the OE derived TCLW and the $N_{\text{pixel_DCC}}$. Note, however, that the variability for both cases is quite large.

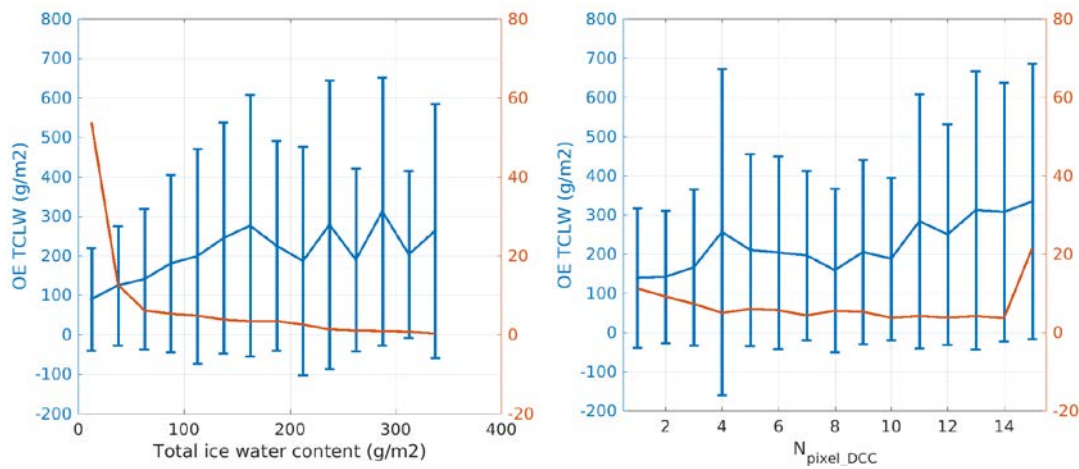


Figure 4-2: OE retrieved total cloud liquid water (TCLW) as a function of TIWP (left) and number of pixels containing deep convective cloud ($N_{\text{pixel_DCC}}$) (right) from 2007-2011. On the left y-axis: solid lines and error bars represent mean and standard deviation of each bin, respectively. The right y-axis shows normalized histogram of bins. A minimum of 30 matchups in each bin is applied for statistics calculation.

4.3 Uncertainty on SST Retrievals

Both the OE and the RE retrievals have an uncertainty associated with each SST. Figure 4-3 shows how the retrieval uncertainty relates to the deep convective clouds, as observed from the CALIOP instrument. It is evident from the figure that there is a relation between the OE SST uncertainty and the $N_{\text{pixel_DCC}}$, where the uncertainty increases with the increasing number of pixels containing DCC. In opposition to this, the uncertainty estimates from the RE retrieval show no relation to the number of pixels affected by DCC conditions.

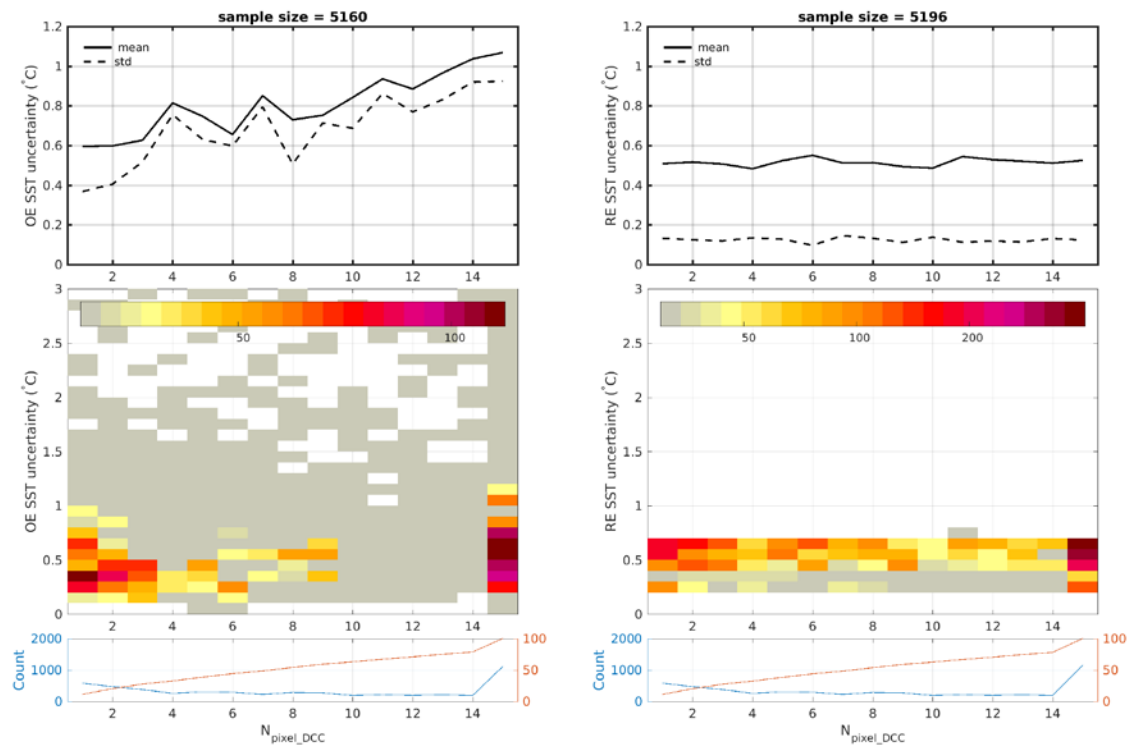


Figure 4-3: SST uncertainty estimates from the retrievals as a function of number of pixels containing deep convective clouds ($N_{\text{pixel_DCC}}$, ranging from 1 to 15) from 2007-2011: OE SSTs (left) and RE SST (right). Top panels: solid and dashed lines are average and standard deviation of uncertainties, respectively. Middle panels: number of matchups in each bin. Bottom panels: the total number of matchups (blue) and the cumulative percentage of matchups (red) in each bin (for 1 pixel). A minimum of 30 matchups in each bin is applied for statistics calculation in the top figures.

In the same way, we compare the two kinds of SST uncertainty estimates to observed TIWP in Figure 4-4. Again, the OE uncertainty is seen to gradually increase with increasing TIWP when TIWP is less than 250 g m^{-2} , whereas no response can be seen from the RE uncertainty. Figure 4-3 and Figure 4-4 thus demonstrate that the uncertainty estimate from the OE SST retrieval is related to the atmospheric impacts from the deep convective cloud and ice clouds, which is not the case for the uncertainties from the RE algorithm and hence the OE algorithm has an advantage over the RE algorithm.

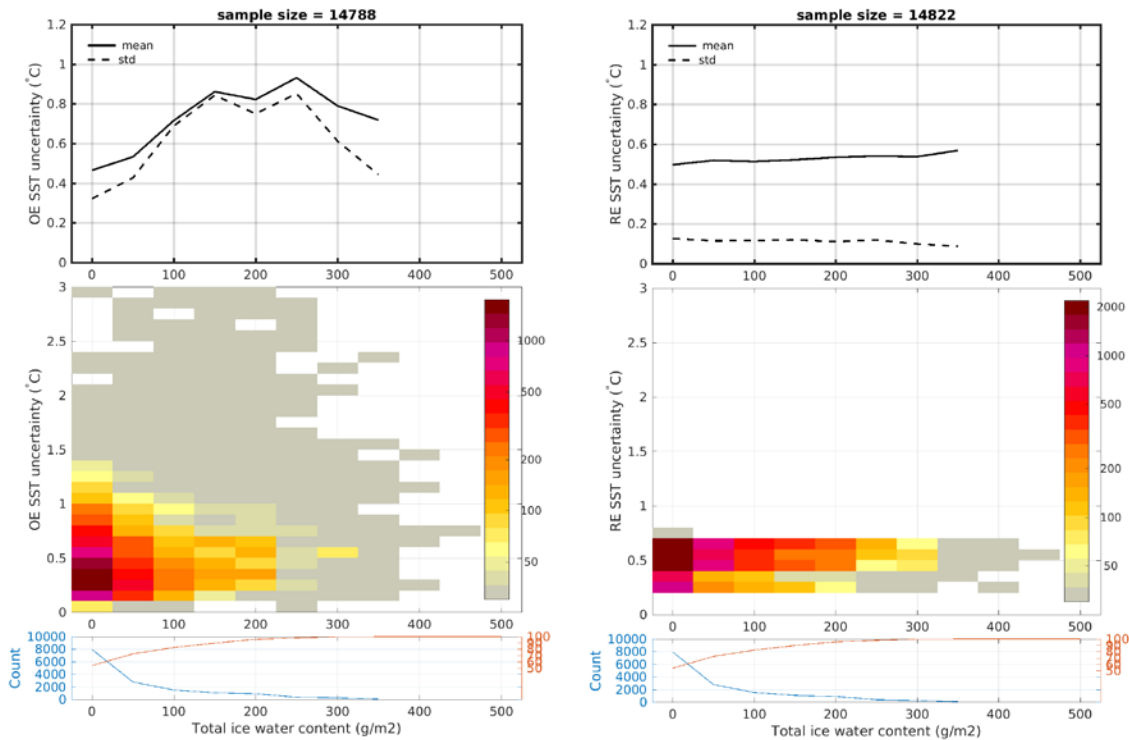


Figure 4-4: SST uncertainty estimates from the retrievals as a function of TIWP from 2007-2011: OE SSTs (left) and RE SST (right). Top panels: solid and dashed lines are average and standard deviation of uncertainties, respectively. Middle panels: number of matchups in each bin. Bottom panels: the total number of matchups (blue) and the cumulative percentage of matchups (red) in each bin (for 1 pixel). A minimum of 30 matchups in each bin is applied for statistics calculation in the top figures.

4.4 Ice Impact on Observations

The direct impact of ice crystals in the atmosphere on the microwave observations is expected to be largest for the 89 GHz channels (Mätzler, 2006). The dependency of the brightness temperature in the 89V channel on TIWP is shown in Figure 4-5 and shows the expected behaviour, where the increasing scattering of the ice crystals in the atmosphere will tend to reduce the brightness temperatures as they will obscure the surface. The average impact on brightness temperatures is again small compared to the variability, but note that the results are shown for surfaces with a large natural variability in temperature.

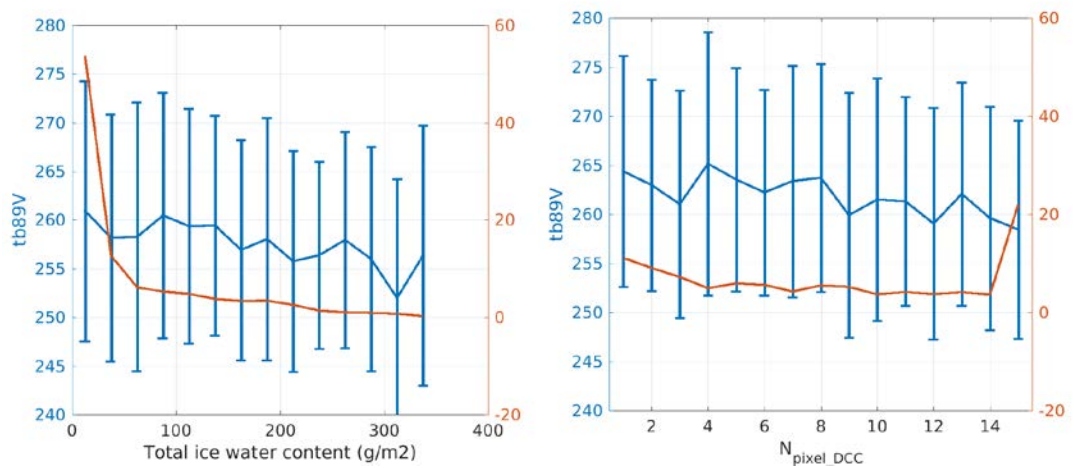


Figure 4-5: AMSR-E brightness temperature of the 89V channel as a function of TIWP (left) and number of pixels containing deep convective cloud ($N_{\text{pixel_DCC}}$) (right) from 2007-2011. On the left y-axis: solid lines and error bars represent mean and standard deviation of each bin, respectively. The right y-axis shows normalized histogram of bins. A minimum of 30 matchups in each bin is applied for statistics calculation.

5. CONCLUSIONS AND RECOMMENDATIONS

5.1 General Concepts

In this work, the AMSR-E SST L2 product was compared with the L2 cloud product from MODIS and CALIOP. The difference in spatial sampling between the three different instruments meant that most of the work was based upon summary variables that were derived to suit the AMSR-E footprint as good as possible. Due to the nature of the CALIOP data with near-nadir only observations, the number of matches in the multi-sensor matchup dataset (MMD) is limited, but it appeared that (except for the aerosols) the results were not very sensitive to the number of matches or the spatial distributions.

In general we only found a small impact from cloud properties on AMSR-E SST retrievals, where the cloud cover from e.g. MODIS had no effects on the quality of the SST retrievals. In addition, no large influence from the presence of aerosols is seen on the quality of the SST retrievals. The direct effects from aerosols on the quality of the SST retrieval is actually opposite, with better retrievals in presence of aerosols, but this was shown to be a sampling effect and not related to the aerosols as observed by CALIOP.

The absence of cloud cover and aerosol effects on the AMSR-E SST retrievals is very encouraging, as this demonstrates that the PMW is an important supplement to IR observations and a valuable part of the global Climate Observing System (GCOS), which requires an all-weather diurnal and high spatial resolution capability with an SST stability of 0.1°C (GCOS, 2006).

There were two key parameters from the CALIOP cloud data that had an impact on the quality of the SST retrievals, namely the number of pixels containing deep convective cloud (DCC) in pixel extract and total ice water content (TIWP). The observed impact from DCCs and TIWP is likely due to the fact that rain and ice are present at the same time in conditions with deep convective clouds. The focus in this report has been on quantifying the effects and establishing relationships to other information that could be used to screen the data.

In order to identify or filter for the SST retrievals that are impacted by the atmospheric effects, it is clear that other cloud products from e.g. MODIS are not suitable for screening the data. In addition, the NWP variables of e.g. total cloud liquid water (TCLW) and TCIW used in this study are not accurate enough to identify the impacted observations. The NWP used in the construction of the MMD is from the ERA Interim analysis times. Using forecast fields would probably give a better representation of the TCLW and TCIWs as it is well known that NWP humidity fields are not the optimal fields. In addition, better atmospheric reanalysis products, such as the ERA5, are emerging that could be investigated in a follow-up study. Using retrieved variables of e.g. TCLW from the OE algorithm instead of the NWP fields showed, however, a better potential for identifying the observations influenced by DCC.

Whereas the OE and RE retrievals showed fairly similar impact on the SSTs of atmospheric effects, such as DCC, the uncertainties had a quite different behaviour. It was clear from the results that the OE uncertainty information was much better at capturing and identifying the conditions where the observations were affected by DCC.

As mentioned earlier, it was shown that the SST retrieval performance is related to the ice content, measured as TIWP by the CALIOP instrument. According to microwave radiation theory (Mätzler, 2006), the major impact from ice on the observations should be seen in the 89 GHz channels, which play a minor role in the SST retrievals. The observed relation between TIWP and SST performance is therefore likely from the fact, that rain and ice are present at the same time in conditions with DCC.

It can therefore be concluded from this study, that the impact from atmospheric effects on the PMW observations is small. This is important, considering the role as supplemental to the IR SST record. The largest effect is seen from deep convective clouds, but the OE retrieval showed some potential in identifying and screening for these effects. It is therefore recommended from this study that more work is done on OE algorithms in order to further develop the uncertainty estimates and to quantify the relation with atmospheric effects such as deep convective clouds.

6. REFERENCES

- Alerskans, E., J. L. Høyer, L. T. Pedersen, C. Gentemann and P. Nielsen-Englyst, 2018: Algorithm Theoretical Basis Document – DMI Regression Model for PMW SST retrievals. ESA CCI SST project report.
- Ackerman, S., K. Strabala, W. Menzel, R. Frey, C. Moeller, and L. Gumley, 1998: Discriminating clear sky from clouds with MODIS. *J. Geophys. Res.*, 103, D24, 32141 – 32157.
- Ashcroft, P., and F. Wentz, 2013: AMSR-E/Aqua L2A Global Swath Spatially-Resampled Brightness Temperatures (Tb), Version 3.
- Atkinson, C., N. Rayner, J. Kennedy, and S. Good, 2014: An integrated database of ocean temperature and salinity observations. *J. Geophys. Res. Oceans*, 119, 7139–7163, doi:10.1002/2014JC010053.
- Baum, B., W. Menzel, R. Frey, D. Tobin, R. Holz, S. Ackerman, A. Heidinger, and P. Yang, 2012: MODIS cloud top property refinements for Collection 6. *J. Appl. Meteor. Clim.*, 51, 1145–1163, doi: 10.1175/JAMC-D-11-0203.1.
- Block, T. 2018: SST CCI Microwave Matchup Data Content Report, SST_CCI-TN-BC-201, WP100 DOP-2, submitted.
- Block, T., S. Embacher, C. Merchant and C. Donlon, 2018: High Performance Software Framework for the Calculation of Satellite-to-Satellite Data Matchups (MMS version 1.2). *Geosci. Model Dev. Discuss.*, doi:10.5194/gmd-2017-54.
- Chang, F., and Z. Li, 2005: A new method for detection of cirrus overlapping water clouds and determination of their optical properties. *J. Atmos. Sci.*, 62, 3993–4009, doi:10.1175/JAS3578.1.
- Davis, S., L. Avallone, B. Kahn, K. Meyer, and D. Baumgardner, 2009: Comparison of airborne in situ measurements and MODIS retrievals of cirrus cloud optical and microphysical properties during the Midlatitude Cirrus Experiment (MidCIX). *J. Geophys. Res.*, 114, D02203, doi:10.1029/2008JD010284.
- Frey, R., S. Ackerman, Y. Liu, K. Strabala, H. Zhang, J. Key, and X. Wang, 2008: Cloud detection with MODIS. Part I: Improvements in the MODIS cloud mask for collection 5. *J. Atmos. Oceanic Technol.*, 25, 1057–1072.
- Gentemann, C. and K. Hilburn, 2015: In situ validation of sea surface temperatures from the GCOM-W1 AMSR2 RSS calibrated brightness temperatures: Validation of RSS GCOM-W1 SST. *J. Geophys. Res. Oceans*, 120, 3567–3585, doi:10.1002/2014 JC010574.
- GCOS 2006: Systematic Observation Requirements for Satellite-based Products for Climate: Supplemental Details to the satellite-based component of the “Implementation Plan for the Global Observing System for Climate in support of the UNFCCC (GCOS-92)”, GCOS-107, September 2006 (WMO/TD No.1338)
- Good, S., M. Martin, and N. Rayner, 2013: EN4: Quality controlled ocean temperature and salinity profiles and monthly objective analyses with uncertainty estimates. *J. Geophys. Res. Oceans* 2013, 118, 6704–6716, doi:10.1002/2013JC 009067.
- Heymsfield, A., D. Winker, and G. van Zadelhoff, 2005: Extinction-ice water content-effective radius algorithms for CALIPSO. *Geophys. Res. Lett.*, 32, L10807, doi:10.1029/2005GL022742.

Holz, R., S. Ackerman, F. Nagle, R. Frey, S. Dutcher, R. Kuehn, M. Vaughan, and B. Baum, 2008: Global MODIS cloud detection and height evaluation using CALIOP. *J. Geophys. Res.*, 113, D00A19, doi:10.1029/2008JD009837.

Hunt, W., D. Winker, M. Vaughan, K. Powell, P. Lucker, and C. Weimer, 2009: CALIPSO lidar description and performance assessment. *J. Atmos. Oceanic Technol.*, 26, 1214–1228, doi: 10.1175/2009JTECHA1223.1

Liu, Z., M. Vaughan, D. Winker, C. Kittaka, B. Getzewich, R. Kuehn, A. Omar, K. Powell, C. Trepte, and C. Hostetler, 2009: The CALIPSO lidar cloud and aerosol discrimination: Version 2 algorithm and initial assessment of performance. *J. Atmos. Oceanic Technol.*, 26, 1198–1213.

Mätzler, C., 2006: Thermal microwave radiation: applications for remote sensing (Vol. 52). *Int. J. Remote Sens.*

Nielsen-Englyst, P., J. Høyer, L. Pedersen and J. Steinwagner, 2017: ATBD - DMI Optimal Estimator for PMW SST retrievals, SST CCI Phase-II.

Nielsen-Englyst, P., J. Høyer, L. Pedersen, C. Gentemann, E. Alerskans, T. Block, and C. Donlon, 2018: Optimal estimation of sea surface temperature from AMSR-E. *Remote Sens.*, 10, 229, doi:10.3390/rs10020229.

O'Carroll, A., J. Eyre, and R. Saunders, 2008: Three-way error analysis between AATSR, AMSR-E, and In situ sea surface temperature observations. *J. Atmospheric Oceanic Technol.*, 25, 1197–1207, doi:10.1175/2007JTECHO542.1.

Sourdeval, O., L. Labonnote, G. Brogniez, O. Jourdan, J. Pelon, and A. Garnier, 2013: A variational approach for retrieving ice-cloud properties from infrared measurements: Application in the context of two IIR validation campaigns. *Atmos. Chem. Phys.*, 13, 8229–8244, doi:10.5194/acp-13-8229-2013.

Wentz, F., and T. Meissner, 2000: AMSR Ocean Algorithm. Algorithm Theoretical Basis Document; Remote Sensing Systems: Santa Rosa, CA.

Winker, D., M. Vaughan, A. Omar, Y. Hu, K. Powell, Z. Liu, W. Hunt, and S. Young, 2009: Overview of the CALIPSO mission and CALIOP data processing algorithms. *J. Atmos. Oceanic Technol.*, 26, 2310–2323.

Woodruff, S., S. Worley, S. Lubker, Z. Ji, J. Freeman, D. Berry, P. Brohan, E. Kent, R. Reynolds, S. Smith, and C. Wilkinson, 2011: ICOADS Release 2.5: extensions and enhancements to the surface marine meteorological archive. *Int. J. Climatol.*, 31, 951–967, doi:10.1002/joc.2103.

7. ACKNOWLEDGEMENT TO CLOUD DATA PROVIDERS

MODIS : ftp://ladsweb.nascom.nasa.gov/allData/6/MYD06_L2/

CALIOP: NASA Langley ASDC User Services (support-asdc@earthdata.nasa.gov),
ordering data via https://eosweb.larc.nasa.gov/HORDERBIN/HTML_Start.cgi

AMSR-E L2A from RSS were obtained from NSIDC at: http://nsidc.org/data/ae_l2a